

Morphological Attributes Govern CO₂ Reduction on Mesoporous Carbon Nanosphere with Embedded Axial Co-N₅ Sites

Youzhi Li

Zhejiang University

Bo Wei

Beihang University

Zhongjian Li

Zhejiang University

Lei Fan

Rice University

Qike Jiang

Dalian Institute of Chemical Physics

Lecheng Lei

Zhejiang University <https://orcid.org/0000-0002-4471-5898>

Ruifeng Zhang

Beihang University

Yingying Lu (✉ yingyinglu@zju.edu.cn)

Zhejiang University

Article

Keywords: single-atom catalysts, CO₂ reduction reaction, density functional theory

Posted Date: October 29th, 2021

DOI: <https://doi.org/10.21203/rs.3.rs-999257/v1>

License: © ⓘ This work is licensed under a Creative Commons Attribution 4.0 International License.

[Read Full License](#)

Morphological Attributes Govern CO₂ Reduction on Mesoporous Carbon Nanosphere with Embedded Axial Co-N₅ Sites

Youzhi Li¹, Bo Wei², Zhongjian Li^{1}, Lei Fan¹, Qike Jiang³, Lecheng Lei¹, Ruifeng Zhang^{2*}, Yingying Lu^{1*}*

¹Y. Li, Prof. Z. Li, L. Fan, Prof. L. Lei, Prof. Y. Lu

College of Chemical and Biological Engineering, Zhejiang University, Hangzhou
310027, China

E-mail: zdlizj@zju.edu.cn (Prof. Z. Li), yingyinglu@zju.edu.cn (Prof. Y. Lu)

²B. Wei, Prof. R. Zhang

Center for Integrated Computational Materials Engineering and Key Laboratory of
High-Temperature Structural Materials & Coatings Technology, Beihang University;
School of Materials Science and Engineering, Beihang University, Beijing, 100191,
China

E-mail: zrf@buaa.edu.cn (Prof. R. Zhang)

³Q. Jiang

Dalian National Laboratory for Clean Energy, Chinese Academy of Sciences, Dalian
116023, China

Abstract

Although single-atom catalysts (SACs) have been widely employed in the CO₂ reduction reaction (CO₂RR), the understanding regarding the effect of morphological attributes on catalytic performance are still lacking, which prevents the rational design of high-performance catalysts for electrochemical CO₂RR. Here, we developed a novel catalyst with axial Co-N₅ sites embedded on controllable mesoporous carbon nanosphere with different graded pore structures. Benefiting from the precise control of porosity, the influence of morphological attributes on catalytic performance was well revealed. In situ characterization combined with density functional theory (DFT) calculations revealed that axial N-coordination induced local d-p orbitals coupling enhancement of Co with oxides and the optimal pore size of 27 nm promoted the interfacial bonding characteristics, which facilitate both the COOH* generation and CO desorption. Consequently, A superior selectivity of nearly 100% at -0.8 V vs. RHE and commercially relevant current densities of >150 mA cm⁻² could be achieved, and a strikingly high turnover frequency of 1.136*10⁴ h⁻¹ at -1.0 V has been obtained, superior to the most of Co-based catalysts.

Introduction

The ever-increasing energy demand accompanied with the excess emissions of greenhouse gases leads to the energy crisis and global warming¹⁻³. Electrochemical reduction of CO₂ provides a viable approach to convert greenhouse gas into value-added products, utilizing renewable energy⁴⁻⁷. The key point of CO₂RR is the construction of electrocatalyst⁸⁻¹¹. Among various candidates, atomically dispersed metal catalyst has received extensive attention and get rapid development for their high atomic utilization, low-cost manufacturing, powerful metal-support interaction and modulating coordination environment, especially for single-site catalyst¹²⁻¹⁵. Despite extensive efforts by researchers, precise control of morphology still remains great challenging. The lacking understanding about the influence of morphological attributes on catalytic performance blocks the rational design of high-performance catalysts for CO₂RR¹⁶.

For single-site catalyst, the selectivity of electrochemical CO₂ reduction is closely related to the modulation of chemical environment in catalyst, the activity, meanwhile, is limited to the atomic utilization derived from the partial exposure of active atoms¹⁷⁻¹⁹. Thus, simultaneously engineering the electronic modification and morphological structure for tuning chemical environment and promoting exposure of active sites open new opportunities to outperform the well-established catalyst. Considering the unfilled 3d orbitals in transition metal-nitrogen co-decorated nanocarbon could enhance the charge transfer between M center and COOH* intermediate, it is a reasonable method

to increase the d-states of M sites to reduce the energy barrier of COOH* formation, which is commonly believed to be an essential pathway for CO production²⁰⁻²³. And thus the selectivity of catalyst could be further optimized. Moreover, the increase of overall activity could be addressed by further improvement to achieve the most efficient utilization of active sites via morphological and structural control of catalyst. Hollow nanostructures combining functional shells and inner voids offer low density, large surface area. Meanwhile hierarchical hollow structures organized by secondary subunits with high-energy facets ensure highly dense exposure of active sites²⁴. Thus the activity would be enhanced. Rationally increasing the complexity of chemical environment and morphological nanostructures will likely endow them with new functionalities and great significance for all kinds of catalytic reaction and other emerging technologies.

Herein, we reported a novel CO₂RR electrocatalyst, in which atomically dispersed Co-N₅ with axially tractive coordination was embedded in adjustable mesoporous carbon nanosphere. The axially tractive Co-N₅ embedded on tortile N-doped carbon induced unique electronic structure, and the mesoporous foam structure promoted the contact between reactant and highly exposed active sites. Benefiting from the precise control of porosity, the influence of morphological attributes on catalytic performance was well revealed. As a result, the superior activity and selectivity have been reached. The rational designed catalyst showed a 96.1% CO faradaic efficiency (F.E.) at -0.8 V vs. RHE, and a remarkably high turnover frequency of $1.136 \times 10^4 \text{ h}^{-1}$ at -1.0 V has been

obtained, which exceeded the most of Co-based catalysts. Commercially relevant current densities of $>150 \text{ mA cm}^{-2}$ also have been achieved in flow cell. The exceptional CO₂RR performance originates from the active moiety with axial oxygen traction and precise control of porosity. Local structures and coordination environment was identified through X-ray absorption fine structure (XAFS) spectroscopy. DFT calculation revealed that axial traction of nitrogen atom produced a stronger d-p orbital coupling, leading to a reduced free energy of COOH*, further resulting in a promoted COOH* generation and CO desorption as well as suppressing the competitive hydrogen evolution reaction. Moreover, In-situ FIIR revealed the interfacial bonding characteristics, the optimal pore size of 27 nm has been obtained, which enhanced both the adsorption and conversion of intermediate for CO₂RR. This work provides an efficient way to tailor and optimize the catalytic activity and selectivity by atomic-scale design and structural control.

Results

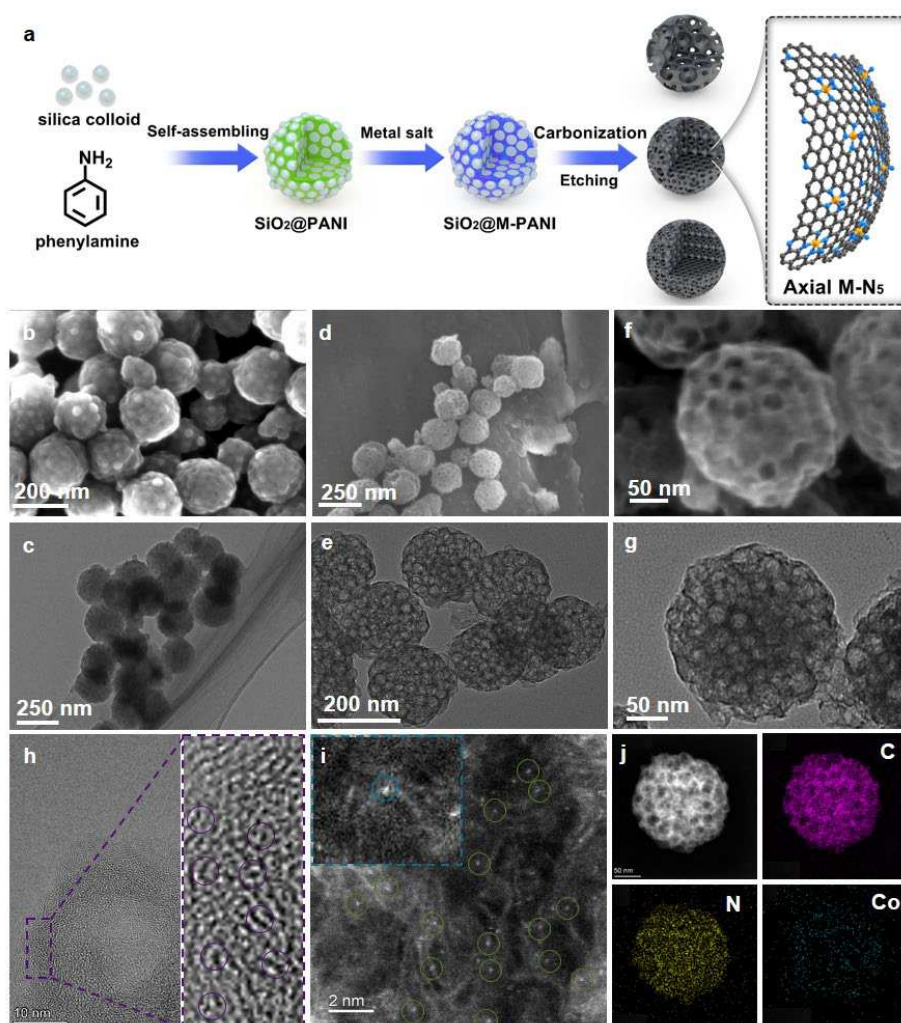
Synthesis and characterizations of Co-MSPNC

As illustrated in Fig. 1a, silica colloid nanoparticles was used as a porosity-inducing template, polyaniline (PANI) was used as C and N sources and cobalt chloride was selected as metal precursors. Silica colloid nanoparticle and polyaniline self-assembled into nanospheres, where Co²⁺ could be coordinated with the amine or imine nitrogen atoms (denoted as SiO₂@Co-PANI). Then, after pyrolysis under an inert atmosphere at high temperature, the coated Co-PANI layers on the resultant SiO₂@Co-PANI

nanospheres carbonized into N-doped carbon and the coordinated Co^{2+} ions were embedded on the walls (denoted as $\text{SiO}_2@\text{M-N-C}$). Eventually, the annealed product was leached in NaOH ethanol aqueous solution to remove the SiO_2 template, resulting in the formation of isolated single Co atoms immobilized on mesoporous N-doped carbon nanosphere (denoted as Co-MSPNC). A uniform spherical structure containing silica colloid nanoparticles could be observed (Fig. 1b-c, Supplementary Fig. 1-3) from scanning electron microscopy (SEM) and transmission electron microscopy (TEM), confirming the intermediate of self-assembled $\text{SiO}_2@\text{PANI}$ during the synthesis procedures. The morphologies of Co-MSPNC were displayed in Fig. 1d-g and Supplementary Fig. 4, the spherical structure inherited the shape of $\text{SiO}_2@\text{PANI}$, while the removing of template leads to formation of uniform pore structure.

HRTEM image (Supplementary Fig. 5) clearly showed that Co-MSPNC had a diameter of about 200nm with plentiful spherical pores due to the removal of silica nanoparticles. The average pore size is about 27 nm and the thickness of wall is at the range of 4nm to 10nm, which depends on the measured positions (Supplementary Fig. 6). No significant nanocrystals or nanoparticles (NPs) were observed throughout the porous nanocarbon, which agrees with the selected area electron diffraction (SAED) observations (Supplementary Fig. 5). The enlarged HRTEM image (Fig. 1h) displayed lattice distortion defects characteristic, which might be attributed to the coordination of single cobalt atoms with nitrogen. In order to confirm the existence Co single sites, the aberration-corrected atomic-resolution high-angle annular dark field scanning

Fig. 1: Synthesis and characterization of Co-MSPNC.



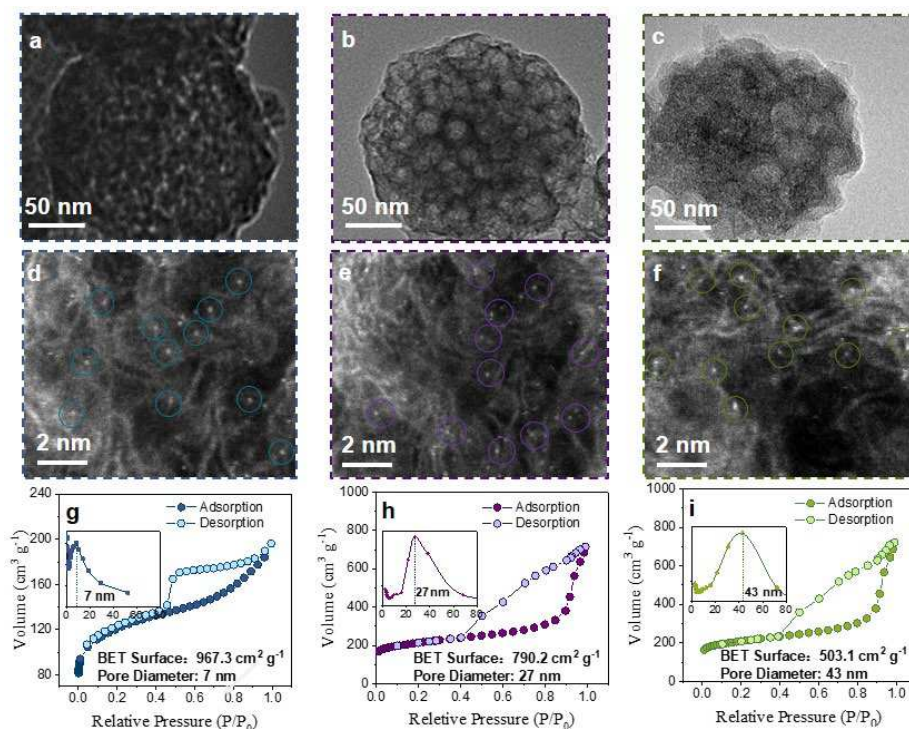
a Schematic illustration of the synthesis process of Co-MSPNC. **b** SEM image and **c** TEM image of SiO₂@PANI, **d-f** SEM image and **e-g** TEM image of Co-MSPNC, **h** HRTEM images, **i** HAADF-STEM image and **j** corresponding EDX mappings of C, N, and Co elements of Co-MSPNC. The color of gray, blue and orange present C, N and Co atom respectively.

transmission electron microscopy (HAADF-STEM) was carried out (Fig. 1i). Serried isolated bright dots evenly distributed on the carbon matrix, which demonstrates that the metal were atomically dispersed. The isolated Co atoms have been marked with green circles for clear observation, and no metal nanoparticles had formed. Notably,

some Co atoms were anchored on curving support, which might lead to unique electronic modulation (inset of Fig. 1i). The elemental mapping acquired by the energy-dispersive X-ray spectroscopy (EDS) manifests homogeneous distribution of Co, N and C over the entire architectures (Fig. 1g, Supplementary Fig. 7), indicating that the single-site anchoring of Co on N doped carbon. The Co loadings are 0.21 wt% through the inductively coupled plasma mass spectrometry (ICP-MS) analyses. Additionally, X-ray diffraction (XRD) was conducted, and two characteristic diffraction peaks at approximately 24° and 44° were displayed in the XRD pattern (Supplementary Fig. 8) and were assigned to the graphite (002) and (100) planes, which further confirms the atomic dispersion of Co with non-formation of massive metallic and oxide crystals on carbon supports²⁵. This result is according with the phenomenon observed in HAADF-STEM image. The relatively high D band-to-G band intensity ratio (I_D/I_G) was calculated to be 1.09 in Raman Spectrum (Supplementary Fig. 9). This result implied its great degree of structural disorder within the catalyst, which may be attributed to the anchor of single cobalt atoms with nitrogen on carbon support.

In order to probe the role of the porosity in the CO₂RR process, we established various Co-N single-site catalyst with different porosity. Different sizes of silica colloid nanoparticles was used as a porosity-inducing template. As shown in Fig. 2a-c, the formation of interconnected carbon structures with uniformly sized pores was verified by HRTEM. The average diameter of the pores (determined from the TEM images) was about 7 nm, 27 nm, and 43 nm for the Co-MSPNC-7, Co-MSPNC-27 and Co-MSPNC-

Fig. 2: Characterization of Co-MSPNC with different graded pore structures.



a-c TEM image, **d-f** HAADF-STEM image, **g-h** N₂ adsorption-desorption isotherm curve of Co-MSPNC-7, Co-MSPNC-27, Co-MSPNC-43, respectively, inset: corresponding pore size distribution.

43 samples, respectively, mirroring the size of the template silica particles. Serried isolated bright dots evenly distributed on the carbon matrix, which demonstrates that the metal were atomically dispersed (Fig. 2d-f). The isolated Co atoms have been marked with different color of circles for clear observation, and no metal nanoparticles had been observed. The N₂ adsorption-desorption isotherm curve of Co-MSPNC showed a high Brunauer-Emmett-Teller (BET) surface area. The pore size distribution curve was calculated from the adsorption branch of the isotherm curve using the Barrett-Joyner-Halenda (BJH) method. N₂ adsorption and desorption isotherms of Co-MSPNC-7 showed dominantly microporous features with the characteristic hysteresis

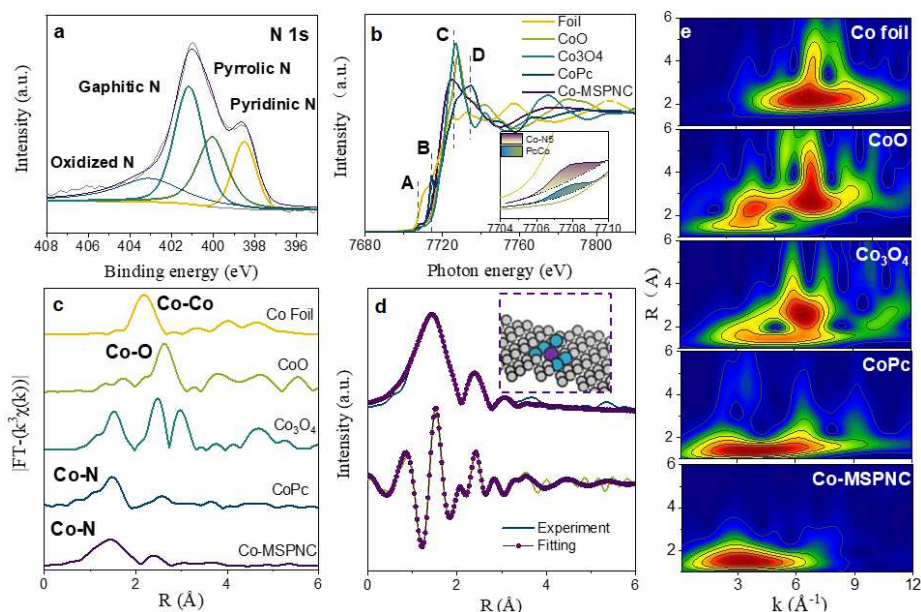
loops, while the Co-MSPNC-27 and Co-MSPNC-43 demonstrates a mesoporous structure. The pore size distribution curves peaked at 7, 27 and 43 nm for each of sample, further confirmed that uniformly size pores formed. Specific surface areas were 967.3 $\text{m}^2 \text{g}^{-1}$ for Co-MSPNC-7, 790.2 $\text{m}^2 \text{g}^{-1}$ for Co-MSPNC-27, 503.1 $\text{m}^2 \text{g}^{-1}$ for Co-MSPNC-43. Variations in the porosity of Co-MSPNC samples can result in distinct differences in both activity and selectivity. The large surface area, plentiful pores and high pore volume pave the way for subsequent catalytic reaction.

The chemical and atomic structure of Co-MSPNC were analyzed using X-ray photoelectron spectroscopy (XPS) and X-ray absorption fine structure (XAFS) spectroscopy measurement. The high-resolution N1s spectra indicates the presence of pyridinic (398.5 eV), pyrrolic (400.2 eV) graphitic (401.6 eV), and N-Ox (403.8eV) species (Fig. 3a). No obvious Si 2p XPS signal was found, indicating that silica colloid nanoparticles have been completely removed (Supplementary Fig. 10)²⁶. The Co 2p centered at 781.7 and 796.8 eV could be observed corresponding to the Co 2p_{1/2} and Co 2p_{3/2} levels, respectively (Supplementary Fig. 10)²⁷. The Co K-edge X-ray absorption near-edge structure (XANES) of Co-MSPNC presents a near-edge absorption energy between Co metal foil and Co₃O₄ references, indicating that the Co average valence is between 0 and +2.6 (Fig. 3b). The XANES spectra of Co-MSPNC contain similar characteristic features to those of CoPc, while differences lie mainly in the relative intensities and edge positions (labelled A–D in Fig. 3b). The inset of Fig. 3b highlights the pre-edge features of the XANES spectra, the integrated pre-edge peak (Peak A at

approximately 7708 eV) intensity of CoPc is weaker than that of Co-MSPNC. The increases in the pre-edge peak intensity in Co-MSPNC indicates the distorted D_{4h} symmetry²⁸. Compared with that observed for CoPc, the transition of Co 1s to 4p_z orbitals (peak B) as a fingerprint for square-planar M–N₄ moieties was very weak in Co-MSPNC, which further confirms that Co-MSPNC was not a typical square-planar M–N₄ structure^{28,29}. Additionally, the peak C and peak D are attributed to the 1s to 4p_{x,y} transitions and multiple scattering processes, respectively²⁹. Co-MSPNC showed larger relative intensity ratios (I_C/I_D) than CoPc, further implying that the Co–N₄ structure was partially distorted due to an additional ligand³⁰. Increased I_C/I_D has been found to correlate well with enhanced oxygen reduction reaction activity. Co-MSPNC is therefore expected to perform good electrocatalytic activities

Furthermore, the Co K-edge Fourier transformed extended XAFS (FT-EXAFS) spectrum of Co-MSPNC was conducted. In Fig. 3c, the Co–Co scattering path vanishing at about 2.18 Å further suggests the atomic-level dispersion of the Co species rather than the crystalline metal structure in the Co-MSPNC. The major peak at 1.44 Å can be assigned to the backscattering of Co–N coordination³¹, further confirming the metal–nitrogen coordination. Meanwhile, wavelet transform (WT)-EXAFS was conducted to probe the adjacent properties of metal atoms, allowing more intuitive comparisons on the radial distance k-space resolution. As shown in Fig. 3e, the WT signal related to Co–Co bond at 6.7 Å⁻¹ in Co foil is not detected in Co-MSPNC, further verifying the absence of Co-containing nanoparticles. The observed intensity maxima at 3.3 Å⁻¹

Fig. 3: Structural analysis of Co-MSPNC.



a High-resolution of N 1s, **b** Co K-edge XANES spectra, **c** Co K-edge k^3 -weighted EXAFS spectra, **d** Fitting curves of the FT-EXAFS spectra for Co-MSPNC, The greyish-white, blue and purple refer to C, N and Co atoms, respectively. **e** Co K-edge WT-EXAFS spectra.

appeared in Co-MSPNC is respectively associated with the Co-N paths. Therefore, Co species was further confirmed as atomically dispersed and co-coordinated with N atoms. To determine the local structure of Co-MSPNC, we established a theoretically optimized bimetal-nitrogen model based on density functional theory (DFT) and fitted FT-EXAFS curves. The EXAFS fitting curves at R-space and k-space are both consistent well with experiment spectra of Co-MSPNC (Fig. 3d). The main peak is the nearest neighbor shell, denoted as first Co-N coordination shell, in the radial distance of about 2.01 Å. The coordination numbers of Co-N are 5.3, which indicates the structure of Co-MSPNC is Co-N₅. The calculated Co-N interaction path fits well with the experimental spectra and the structural parameters of coordination numbers (CN),

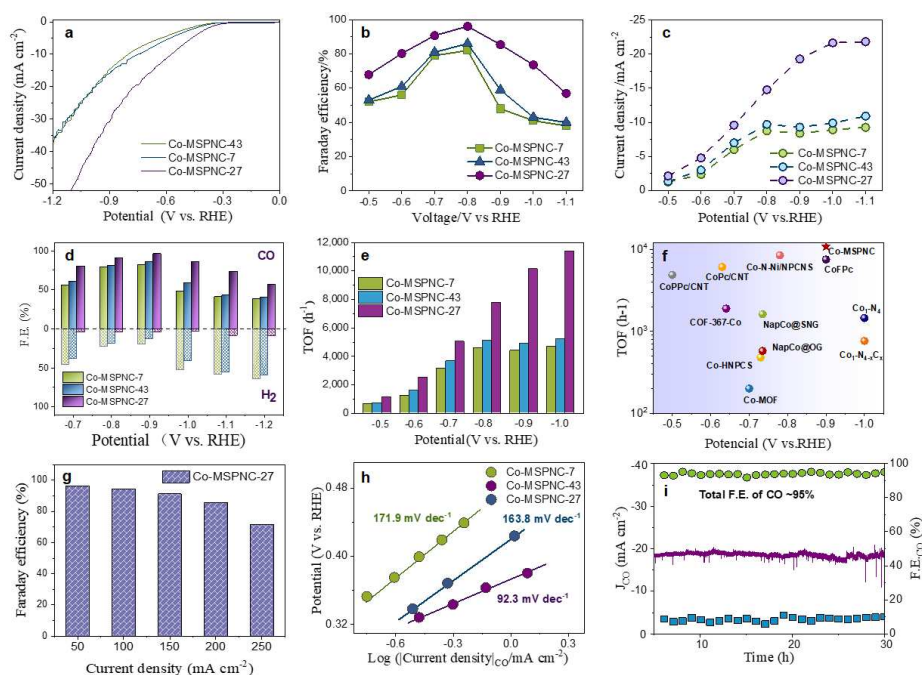
bond distances (R), and Debye-waller factor (σ^2) are listed in Supplementary Table 1. Based on the distorted D_{4h} symmetry and high fitting qualities (low R-factor) of the EXAFS, the isolated Co sites are determined to be inlaid in N-doped carbon with four square-planar Co-N bonds and one axial Co-N bond in a distorted structure.

Electrocatalytic CO₂ reduction performance

Inspired by the unique structural features, we tested the electrocatalytic CO₂RR performance of Co-MSPNC in a two-compartment H-cell with a common three-electrode system. 0.5 M CO₂ saturated KHCO₃ aqueous solution are employed as electrolyte. All potentials in this work were versus the reversible hydrogen electrode (RHE). As revealed by linear sweep voltammetry (LSV) in Fig. 4a and Supplementary Fig. 11, Co-MSPNC-27 displayed the highest total current density from 0 V to -1.2 V and present a low potential of -0.56 V to achieve a current density of -10 mA cm⁻², whereas Co-MSPNC-43 and Co-MSPNC-7 required higher potentials of -0.75 V and -0.81 V to reach the same current density, indicating the superior CRR activity of Co-MSPNC-27. Besides, Co-MSPNC-27 exhibited lower onset potential of CO₂ reduction than that of Co-MSPNC-43 and Co-MSPNC-7. The liquid and gas products were quantified by nuclear magnetic resonance and on-line gas chromatography, which indicate that CO and H₂ are two major products (Supplementary Fig. 12). In Fig. 4b, Co-MSPNC-27 showed a high CO F.E. of 96.1% at a very low potential of -0.8 V. By comparison, only 85.7% and 82.6% CO F.E. were obtained for Co-MSPNC-43 and Co-MSPNC-7 at the same potential, further demonstrating the high selectivity of Co-

MSPNC-27. The superior CO selectivity of Co-MSPNC could be attributed to the tuned electronic structure induced by axial coordination at distorted support. Further, a high CO partial current density (J_{CO}) of 21.68 mA cm⁻² could be reached at -1.0 V for Co-MSPNC-7, roughly 2.19 and 2.46 times higher than that of Co-MSPNC-43 (-9.89 mA cm⁻²) and Co-MSPNC-7 (-8.80 mA cm⁻²) (Fig. 4c), respectively. Meanwhile, a low H₂ F.E. of < 10% was achieved on Co-MSPNC-27 at -0.5 V to -1.0 V, much lower than that of Co-MSPNC-43 and Co-MSPNC-7 (Fig. 4d), reinforcing the pivotal impact of axial Co-N coordination and porous morphology on enhance CRR performance. The enhanced activity of the catalyst is further disclosed by the calculation of the turnover frequency (TOF) based on the number of metal atoms involved in the reaction (Fig. 4e). The Co-MSPNC-27 showed larger calculated TOFs than that of Co-MSPNC-43 and Co-MSPNC-7 across the entire potential window from -0.5 to -1.0 V. Notably, such a high TOFs of Co-MSPNC reported here was among the best relative to all of the previously reported Co-based CRR electrocatalysts (Fig. 4f, Supplementary Table 6)³¹⁻⁴¹. In view of the low solubility of CO₂ aqueous electrolytes, the CO₂RR performance of a gas diffusion electrode (GDE) with loaded Co-MSPNC-27 was further studied, where CO₂ molecules diffused directly to the catalyst from the back of GDE, thus completely removing the mass-transport limitation of solution phase reaction. As shown in Fig 4g, the Co-MSPNC-27 reached a high current density of 150 mA cm⁻² at -1.76 V with a CO FE of >90%. Co-MSPNC presents a low Tafel slope of 92.3 mV dec⁻¹ for CO generation, which was significantly smaller than that of Co-MSPNC-43 (163.8 mV dec⁻¹) and Co-MSPNC-7 (171.9 mV dec⁻¹) (Fig. 4h). This reveals that the

Fig. 4: Electrochemical CO₂ reduction performance of Co-MSPNC.



a LSV curves, **b** CO F.E., **c** CO partial current densities, **d** product distribution and **e** TOFs. **f** TOF of a series of Co-based catalysts combined with Co-MSPNC. **g** CO F.E. for Co-MSPNC-27 under different current densities in flow cell. **h** Tafel plots for CO. of Co-MSPNC-7, Co-MSPNC-27 and Co-MSPNC-43, **i** 30 h electrolysis tests of Co-MSPNC-27 at -0.8 V. The green, blue and purple curves present F.E._{CO}, F.E._{H₂} and current density respectively.

first electron transfer, which generates the surface-adsorbed *COOH intermediate, is the rate-determining step during CO₂RR³⁹. The significantly lowered Tafel slope of Co-MSPNC-27 indicates the kinetics of this step is greatly enhanced. Lower charge-transfer resistance of Co-MSPNC-27 than that of Co-MSPNC-43 and Co-MSPNC-7 could be observed through electrochemical impedance spectroscopy (EIS), suggesting a fast charge-transfer capacity during the CRR process (Supplementary Fig. 13). Furthermore, Co-MSPNC-27 has the larger double-layer capacitance (Cdl) values of

17.1 mF cm⁻² than those of Co-MSPNC-43 (9.54 mF cm⁻²) and Co-MSPNC-7 (3.9 mF cm⁻²), demonstrating the Co-MSPNC-27 have larger electrochemical active surface area (ECSA, Supplementary Fig. 14) than control samples. A stable current density at about -18.0 mA cm⁻² was maintained during a 30h potentialstatic test of Co-MSPNC-27 (Fig. 4i). The structures of Co-MSPNC-27 after performance testing and stability test was well characterized by TEM, HADDF-TEM, XRD, Raman and XAFs (Supplementary Fig. 15), which demonstrates the maintaining of mesoporous nanosphere and axial Co-N₅ structure. Therefore, obvious enhanced CO₂RR performance has been observed on mesoporous carbon nanosphere with the pore size of 27 nm and axial Co-N₅ sites.

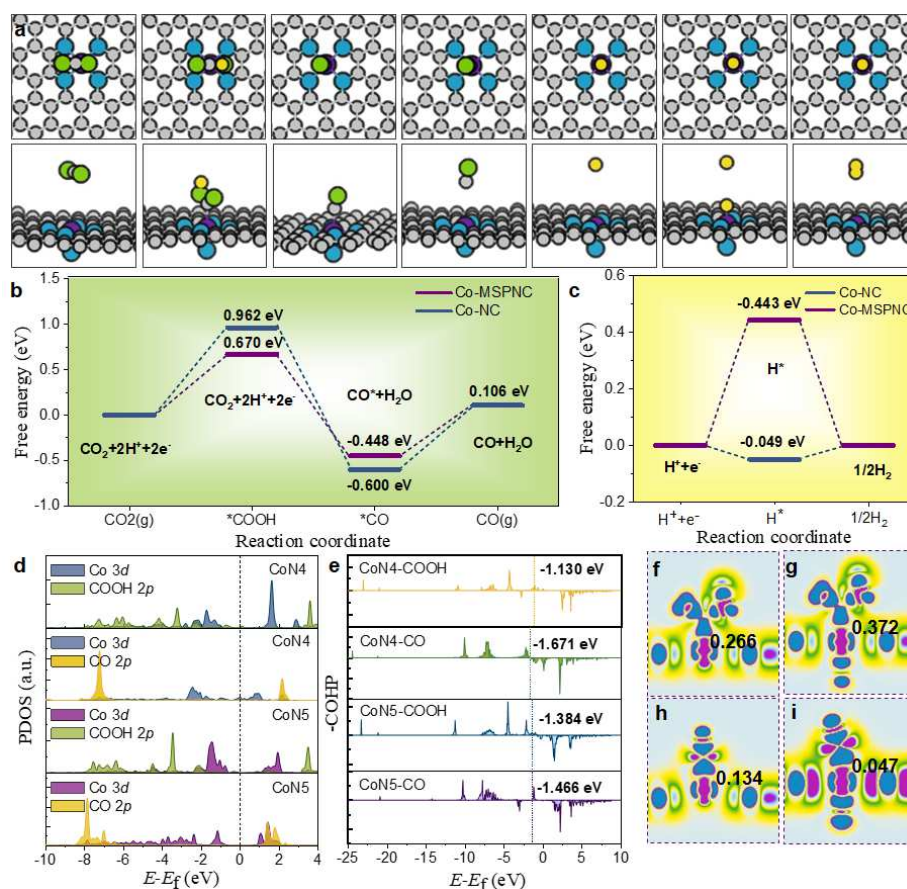
Intrinsic property of the Co-MSPNC catalysts.

To elucidate the key role axial Co-N played in the active Co-MSPNC for the CO₂RR catalytic properties, we adopted the computational hydrogen electrode (CHE) model to calculate the free energy (G) of each intermediate state for the CO₂RR. Besides, we calculated formation energies (ΔE) of Co-N₅ and Co-N₄ structures. The Co-N₅ system has the lower energy than Co-N₄, so the atoms tend to form Co-N₅ (Supplementary Fig. 16). According to the computational hydrogen electrode (CHE) model, the stepwise atomic structures of the CO₂RR process for the electrochemical reduction of CO₂ to CO and the HER process for the reduction of H⁺ ions to H₂ are shown schematically in Fig. 5a. The free energy diagrams for the CO₂RR to CO and HER at U = 0 V (vs RHE) are shown in Fig. 5b, presenting the free energy of each intermediate state on the metal

atom sites in flat Co-N₄-C and axial Co-N₅ sites, and each step represents the transfer of one proton-electron pair. As shown, the free energy barriers (ΔG) for the whole reaction are 1.12 eV and 1.56 eV for Co-MSPNC and Co-N-C, respectively. The reason for this difference is that axial Co-N₅ coordination can significantly decrease the free energy for the *COOH reaction, which is typically thought of as rate-determining step during CO₂RR. Furthermore, the increase of free energy for *CO indicates that axial Co-N₅ coordination facilitates the desorption of CO, leading to a high CO selectivity. Additionally, the remarkably high positive free energy change required (0.44 eV) for the formation of adsorbed hydrogen intermediates during the dominant competitive HER (Fig. 5c) suggested the preferred high selectivity toward CO rather than H₂. Therefore, the introduction of axial Co-N₅ coordination can not only promote the CO₂RR but also maintain the inhibition of the competitive side reaction of the HER, which is in good agreement with the experiments

Further we also calculated formation energies in axial N atoms to evaluate whether the exposed N atom is active for CO₂RR. The free energy for the *COOH reaction in N atom is 7.376 eV, which is much higher than that in Co (0.670 eV). There is a great deal of difference between the two atoms. The almost 10 times of free energy more than Co atom reflect that the exposed N atom is almost non-active for CO₂RR (Supplementary Fig. 17). In order to gain in-depth insights into the catalytic selectivity and the role of axial Co-N coordination, their electronic structures were further investigated. Firstly, the density of states (DOS), the crystal orbital Hamilton population (COHP) and their

Fig. 5: DFT calculations



a the atomic structures of the CO₂RR and HER process. **b-c** The free energy of each intermediate state on the metal atom sites in Co-MSPNC and Co-N₄. **d** Projected DOS (PDOS) for Co 3d orbitals and oxide 2p orbitals including COOH* and CO*. **e** The -COHP and the relative ICOHP values between the metal atoms and the C atoms in the intermediate of each step. **f-g** Valence charge density difference for COOH* on Co-N₄ and Co-MSPNC, **h-i** CO* on Co-N₄ and Co-MSPNC.

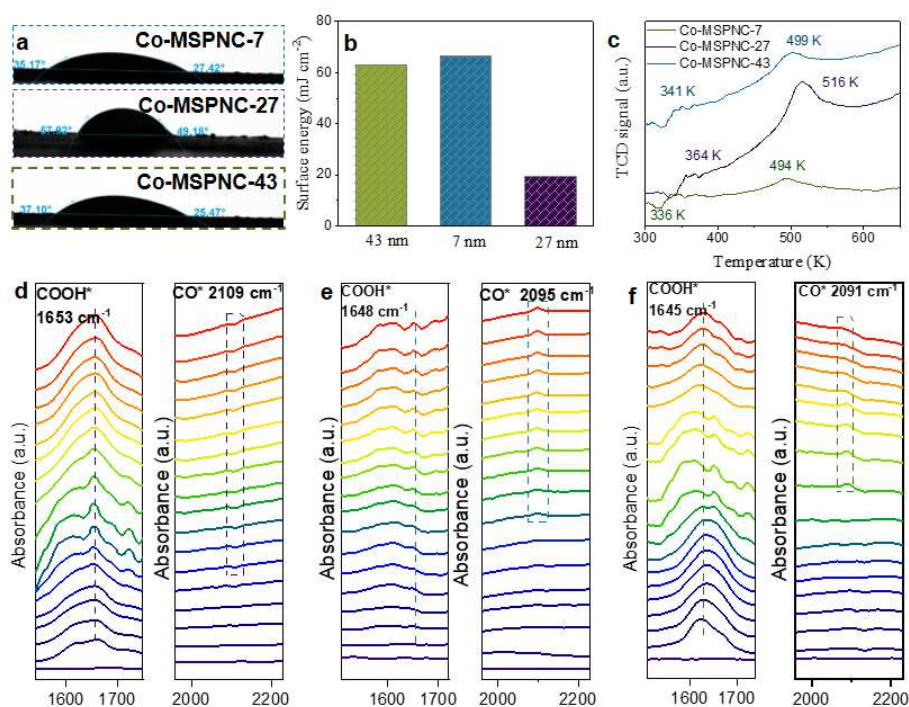
integrated-COHP (ICOHP) values for Co 3d orbitals and the oxide 2p orbitals. There is a negative correlation between the ICOHP value and the strength of d-p interaction, that is, a more negative ICOHP leads to a stronger d-p coupling⁴². For the *COOH step, the *COOH (2p) orbitals are strongly bonded with the Co (3d) orbitals on the Co site

in Co-N₅ because of their relatively bigger DOS overlap and more negative ICOHP value compared with those in Co-N₄. Therefore, the interaction between the Co atom and C atom in COOH* is the stronger than Co-N₄-C, consisting with its lower free energy. For the *CO step, the Co 3d electronic state in Co-N₅ is further from E_F than that of Co-N₄ (Fig. 5d) and the ICOHP value of Co-MSPNC is significantly reduced to -1.466 eV (Fig. 5e), in agreement with its relatively low free energy to promote the CO desorption on axial Co-N₅ sites. Additionally, to better visualize the electron transfer during the catalytic process, valence charge density difference (VCDD) and bader charge transfer number (Δe) were calculated. Fig. 5f-i presents axial traction of nitrogen atom produced an electron-pushing effect, leading to more significant charge polarization on Co-N₅ sites. The larger charge transfer number demonstrates that axial Co-N₅ sites can much more easily adsorb and bond with COOH than Co-N₄-C, while the smaller bader charge for CO* step implies the promoting desorption of CO on axial Co-N₅ sites. These results are consistent with DOS and COHP analysis.

Interfacial analysis of Co-MSPNC with different graded pore structures.

Besides the stronger d-p orbitals coupling activated by axially tractive Co-N₅ sites, the porous structure also plays a significant role during the electrochemical reduction of CO₂. The superior CO selectivity of Co-MSPNC-27 suggests the variations in the porosity could affect the electrocatalytic performance, and 27 nm is the optimal pore size. Considering the porosity directly affect the surface properties, the wetting properties of three samples were investigated by measuring the dynamic (advancing and receding)

Fig. 6: Interfacial property characterization of Co-MSPNC.



a Contact angles, **b** Surface energies, **c** Temperature-programmed CO₂ desorption profiles of Co-MSPNC-7, Co-MSPNC-27 and Co-MSPNC-43 relatively. **d-f** In situ FTIR spectra for the co-adsorption of Co-MSPNC-27, Co-MSPNC-43 and Co-MSPNC-7 relatively.

contact angles of the thin layers. The surface energies (Fig. 6a) were calculated from the contact angle hysteresis. As shown in Fig. 6b, the Co-MSPNC-27 catalyst was the most hydrophobic and presented the lowest hysteresis, resulting in the lowest surface energy ($\gamma_{gs,tot} \sim 19.47 \text{ mJ m}^{-2}$)^{43,44}. Temperature-programmed desorption was employed to study the CO₂ adsorption strength of the catalysts (Fig. 6c). While only one desorption peak was present in case of the Co-MSPNC, CO₂ desorption from the porous samples happened in two distinct steps. We assume that the first step at a lower temperature (< 400 K) is connected to the adsorbed CO₂ on the outer surface of the catalyst layers, and the second step is linked to the desorption of CO₂ from the inner surface of the pores.

The temperature of the desorption from the pores was the highest (516 K) for Co-MSPNC-27, implying the highest CO₂ adsorption strength. Also in the CO₂ conversion, we assume a link between the CO₂ adsorption and reduction activity. Considering that the studied Co-MSPNC catalysts are practically identical in terms of Co-N-containing moieties, we suggest that the distinct CO₂ adsorption strengths arise from the differences in the pore structure. In this case, the strain induced on the CO₂ adsorption sites by the differently curved surfaces is optimal for the 27 nm pores. In order to further understand the reaction pathway and verify the difference in adsorption properties towards reactive intermediates during the CO₂ conversion, in situ Fourier transform infrared (FTIR) spectroscopy was performed. Figure 6d-e presents the FTIR spectra of Co-MSPNC-27, Co-MSPNC-43, and Co-MSPNC-7, respectively, in a CO₂-saturated 0.5 M KHCO₃ electrolyte at stepwise increasing potentials. These three samples all show absorption bands at ~1650 cm⁻¹ that are attributed to *COOH, bands at ~2090 cm⁻¹ that are characteristic of linearly bonded CO⁴⁵. The surface-adsorbed *CO species show distinct evolution trends, which initiate at -0.15 V vs. RHE for Co-MSPNC-27 but occur at a more negative potential of -0.35 and -0.4 V vs. RHE for Co-MSPNC-43 and Co-MSPNC-7, respectively, indicating a weaker adsorption and more difficult process to produce *CO. The adsorbed *COOH species, which are regarded as the crucial intermediates during the reduction of CO₂ to CO, begin at a low potential of approximately -0.05 V vs. RHE for all three samples. As the conversion of *COOH to *CO is thermodynamically downhill, we speculate that Co-MSPNC-27 shows stronger *COOH adsorption than Co-MSPNC-43 and Co-MSPNC-7.

Discussion

In summary, we report the rational design of an axial Co-N₅ sites embedded on controllable mesoporous carbon nanosphere with different pore sizes. Single site was confirmed by aberration-corrected electron microscopy and X-ray absorption spectroscopy. Benefiting from the precise control of porosity, the influence of morphological attributes on catalytic performance was well revealed. The optimized Co-MSPNC-27 possessed a high CO₂RR catalytic selectivity and activity due to its unique electronic modification and morphological structure. A superior selectivity of nearly 100% at -0.8 V vs. RHE could be achieved, and a remarkably high turnover frequency of $1.136 \times 10^4 \text{ h}^{-1}$ at -1.0 V has been obtained, exceeding the most of Co-based catalysts. A high current density of 150 mA cm^{-2} at -1.76 V with a CO F.E. of >90% has been reached. Axial N-coordination modified the d-states of the metal atom and induced local d-p orbitals coupling enhancement of Co with oxides, leading to a reduced free energy of COOH*, further resulting in a promoted COOH* generation and CO desorption as well as suppressing the competitive hydrogen evolution reaction toward a high selectivity of CO production. In-situ FIIR revealed the enhancement of both the adsorption and conversion of intermediate with optimal pore size of 27 nm for CO₂RR. Our results pave the way for the design of novel SACs with a tunable local environment and morphological structure for a wide range of energy and environment related applications.

Methods

Synthesis of Co-MSPNC-27:

0.4g phenylamine (Alfa Aesar) and 1.6g silica colloid (Ludox AM-40) solution initially added into 100ml deionized water. Aqueous HCl solution (1.2 M) was added dropwise to the above-prepared solution until the pH of the solution was 3. After being vigorously stirred for an hour, 0.52g $(\text{NH}_4)_2\text{S}_2\text{O}_8$ (Sinopharm Chemical Reagent Co. Ltd. (China)) dissolved in 4mL distilled water was added into mixed solution and star polymerization for 12 hours at room temperature. $\text{SiO}_2@\text{PANI}$ nanoparticle was obtained by centrifugation. After washing with deionized water and ethanol, $\text{SiO}_2@\text{PANI}$ was added into 1 M aqueous ammonia solution. After stirring for 12 h at room temperature, the product was collected by centrifugation, washed by deionized water for three times and dried at 80 °C for overnight. Subsequently, 225 mg of the above product was added to 10 mL of nitromethane (Maclin Biochemical Co. Ltd.), 0.005 mmol of $\text{CoCl}_2\cdot 6\text{H}_2\text{O}$ was added into the above solution under stirring for 12 hours at room temperature. $\text{SiO}_2@\text{M-PANI}$ was obtained centrifugation, washing and drying. Next, sample was transferred into a quartz tube, which was then heated to 900 °C kept for 3 hours at a heating rate of 5°C/min in flowing argon atmosphere. The sample was collected and soaked in 3 M NaOH $\text{H}_2\text{O}/\text{EtOH}$ (v: v = 1: 1) solution at 100 °C overnight, and then washed with copious deionized water and ethanol, dried at 70 °C under vacuum for overnight. The obtained material was directly used without further treatment.

Synthesis of Co-MSPNC-7:

The Co-MSPNC-7 was prepared with the same procedure as that of Co-MSPNC-27 except the using of silica colloid (The grain diameter is 7nm).

Synthesis of Co-MSPNC-43:

The Co-MSPNC-7 was prepared with the same procedure as that of Co-MSPNC-27 except the using of silica colloid (The grain diameter is at the range of 40-50nm).

Electrode

A three-electrode configuration was used for CO₂RR measurements. To prepare the working electrode, 10 mg of catalyst was dispersed into 100 μ L of Nafion solution (0.5 wt.%) and 900 mL of ethanol by ultrasonic for 2 h and stirring overnight to form a homogeneous ink, and then 100 μ L of as-prepared ink was dropped onto the carbon paper with reactive area of $1 \times 1 \text{ cm}^2$, with a loading amount of 1.0 mg cm^{-2} . Platinum foil was served as counter electrode, and an Ag/AgCl(filled with saturated KCl solution) electrode was acted as reference electrode. All potentials were recorded against an Ag/AgCl reference electrode and converted to versus RHE with iR corrections.

Characterizations

The morphologies of samples was performed by field-emission scanning electron microscopy (FESEM, SU-8010), transmission electron microscopy (TEM, HT7700 120 kV), high-resolution TEM (HRTEM, 200 kV, JEM-2100), and high-angle annular dark field scanning transmission electron microscopy(HAADF-STEM,JEOL JEM-

ARM200F). XRD (ZETIUM DY 2186, 4 kW) was applied to determine the crystal structure, copper target was used in the measurement of XRD pattern. And we get the pattern on 10*10 mm platform with about 0.3g sample. X-ray photoelectron spectroscopy (XPS) of samples was tested on Escalab 250 Xi XPS with an Al K α X-ray resource (Thermo Fisher Scientific). The Brunauer-Emmett-Teller surface area of samples were performed by specific surface area and mesoporous analyzer (TriStar II). The X-ray absorption fine structure spectra (Fe K-edge) were collected at 1W1B station in Beijing Synchrotron Radiation Facility (BSRF). The storage rings of BSRF was operated at 2.5 GeV with an average current of 250 mA. Using Si(111) double-crystal monochromator, the data collection were carried out in transmission/fluorescence mode using ionization chamber. All spectra were collected in ambient conditions. In situ FTIR spectra were acquired using a PerkinElmer spectrum100. All spectroscopic experiments are conducted at a 4 cm⁻¹ spectral resolution and 16 scans.

XAFS Analysis and Results:

The acquired EXAFS data were processed according to the standard procedures using the ATHENA module implemented in the IFEFFIT software packages. The k³-weighted EXAFS spectra were obtained by subtracting the post-edge background from the overall absorption and then normalizing with respect to the edge-jump step. Subsequently, k³-weighted $\chi(k)$ data of Fe K-edge were Fourier transformed to real (R) space using a hanning windows ($dk=1.0 \text{ \AA}^{-1}$) to separate the EXAFS contributions from different coordination shells. To obtain the quantitative structural parameters around

central atoms, least-squares curve parameter fitting was performed using the ARTEMIS module of IFEFFIT software packages.

Electrochemical measurements

Electrochemical measurements were conducted in a traditional H-type cell with a cation exchange membrane (Nafion 117) on electrochemical workstation (Ametek 1470E). The working electrode was carbon paper ($1 \times 3 \text{ cm}^2$) with electrocatalyst. Platinum foil was served as counter electrode, and an Ag/AgCl electrode was acted as reference electrode. The CO₂ or Ar saturated electrolyte was formed by bubbling CO₂ (or Ar as a control) into electrolyte (0.5 M KHCO₃) at least 30 min before CRR test. During the electrochemical measurements, the rate of gas maintained at 20 mL min⁻¹. The polarization curves were measured with a constant rate of 5 mV s⁻¹. The electrochemically active surface area (ECSA) was tested between -0.9V ~ -1.0 V (vs. Ag/AgCl). Electrochemical impedance spectroscopy (EIS) was performed in a frequency range from 10⁵ Hz to 0.01 Hz. Gaseous and liquid products were quantified by gas chromatograph (Agilent GC7820) and ¹H nuclear magnetic resonance (BRUKER AVNCE III500M), respectively.

Density Functional Theory (DFT) Calculations

Spin-polarized DFT calculations were performed using the Vienna ab initio simulation package (VASP) code. Projector augmented wave (PAW) pseudopotential was used to describe the core electrons and a plane wave basis set with a kinetic energy

cutoff of 520 eV was used to expand the wave functions. Electronic exchange and correlation were described within the framework of generalized gradient approximation (GGA) of the Perdew, Burke and Ernzerhof (PBE) exchange-correlation functional. All electronic structure calculations were performed spin-polarized. The convergence of energy and forces were 1×10^{-5} eV and $0.005 \text{ eV \AA}^{-1}$, respectively. The dispersion-corrected DFT-D3 method was adopted to describe the van der Waals (vdW) interactions. The entropic correlation and zero-point energy have been considered in Gibbs free energy calculation. And the implicit solvation model (VASPsol) was used to examine the water-solvent effect on CO, COOH, H adsorbed on the N-doped graphene which adds implicit aqueous electrolyte into the system.

To simulate N-doped graphene supported Co-N₄ and Co-N₅ catalysts, a 7×7 graphene supercell with 98 carbon atoms was chosen. Periodic boundary conditions were employed along x and y directions with a vacuum region of 20 Å between graphene layers. The supercell is large enough to avoid the interaction between the adsorbate and its image. A $5 \times 5 \times 1$ Monkhorst-Pack grid of k-points was used to sample the first Brillouin zones of the surfaces for structural optimizations, while a $6 \times 6 \times 1$ grid of k-points was used for electronic states analysis. All atoms are fully relaxed during structural optimizations.

Computational Hydrogen Electrode (CHE) Model

The computational hydrogen electrode method developed by Nørskov was used to calculate the free energy of each intermediate state. Theoretically, the reaction pathway in the electrochemical reduction of CO₂ to CO following the progress:



in which the asterisk refers to the clean catalysis, and the asterisk-marked one refers to the species that adsorbed on the activity center. In the CHE, the chemical potential of a proton-electron pair, the free energy of $(\text{H}^+ + \text{e}^-)$ equals to $1/2 \text{H}_2(\text{g})$ for the reversible hydrogen electrode (RHE), that $G[\text{H}^+ + \text{e}^-] = 1/2G[\text{H}_2] - eU$, where U is the electrochemical potential relative to RHE. As the initial state (gaseous CO_2 freely above an empty substrate) for the reference, the Gibbs free energy changes of interest can be given by,

$$\Delta G_1 = G[\text{COOH}^*] - G[\text{CO}_2(\text{g})] - G[*] - 1/2G[\text{H}_2] - eU \quad (4)$$

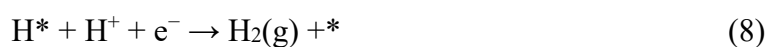
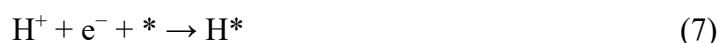
$$\Delta G_2 = G[\text{CO}^*] + G[\text{H}_2\text{O}] - G[\text{COOH}^*] - 1/2G[\text{H}_2] - eU \quad (5)$$

$$\Delta G_3 = G[\text{CO}] + G[*] - G[\text{CO}^*] \quad (6)$$

The CHE model has been used for free energy of adsorbates that involves proton-electron transfers as: $\Delta G(U) = \Delta G_0 + neU$, where n is the number of protons-electrons transferred, U is the potential versus the RHE, ΔG_0 is the maximum free energy at $U=0$.

The limiting potential (U_L) is calculated by: $U_L = -\Delta G_0/e$.

In addition, hydrogen evolution reactions (HER) consists of coupled e^- and H^+ transfers:



and Gibbs free energy changes are shown as below:

$$\Delta G_7 = G[\text{H}^*] - G[*] - 1/2G[\text{H}_2] - eU \quad (9)$$

$$\Delta G_8 = G[\text{H}_2] + G[*] - G[\text{H}^*] - 1/2G[\text{H}_2] - eU \quad (10)$$

The above mentioned Gibbs free energy (G) of a species is calculated according to

$$G = E_{DFT} + E_{ZPE} - TS + \Delta E_{sol} + \Delta H_T \quad (11)$$

where E_{DFT} is the DFT calculated energy change, E_{ZPE} is the zero-point energy, ΔE_{sol} is the solvation energy, ΔH_T is the temperature enthalpy correction from 0 to T K, calculated by the vibrational heat capacity integration $\int_0^T C_p dT$, and TS is the entropy at 298.15 K derived from partition functions and compared with the data from the NIST standard reference database. ZPE corrections were calculated as $E_{ZPE} = \sum_i \frac{1}{2} h\nu_i$, where h is Planck constant and ν_i is the frequency of the i th vibrational mode of binding molecules. In order to account for the gas-phase errors encountered with PBE exchange-correlation functionals to ensure the calculated reaction free energy agrees with the experiments, thermodynamic corrections (ΔH_G) of -0.51, +0.13, -0.08, -0.06 eV were applied for CO, CO₂, H₂, H₂O respectively, suggested by the previous study.

The reversible potential of the overall half-cell reaction:



which energy calculated from DFT is -0.09 eV vs RHE, in agreement with the experiment value -0.11V vs RHE.

The corrections and calculated free energy of gas-phase were listed in Supplementary Table 2. Calculated electronic energy, enthalpy temperature correction, entropy, and free energy of each CO₂RR intermediate at 0 V (vs. RHE) were listed in Supplementary Table 3.

Data Availability

The data that support the plots within this paper and other findings of this study are available from the corresponding authors upon reasonable request.

References

1. Hepburn, C. et al. The technological and economic prospects for CO₂ utilization and removal. *Nature* 575, 87-97, (2019).
2. De Luna, P. et al. What would it take for renewably powered electrosynthesis to displace petrochemical processes? *Science* 364, eaav3506, 3506 (2019).
3. García de Arquer, F. P. et al. CO₂ electrolysis to multicarbon products at activities greater than 1 A cm⁻². *Science* 367, 661-666, (2020).
4. Zhang, W. et al. Atypical Oxygen-Bearing Copper Boosts Ethylene Selectivity toward Electrocatalytic CO₂ Reduction. *J. Am. Chem. Soc.* 142, 11417-11427, (2020).
5. Birdja, Y. Y. et al. Advances and challenges in understanding the electrocatalytic conversion of carbon dioxide to fuels. *Nat. Energy* 4, 732-745, (2019).
6. Zhong, M. et al. Accelerated discovery of CO₂ electrocatalysts using active machine learning. *Nature* 581, 178-183, (2020).
7. Wang, Y. et al. Regulating the coordination structure of metal single atoms for efficient electrocatalytic CO₂ reduction. *Energy Environ. Sci.* 13, 4609-4624, (2020).
8. Ager, J. W. & Lapkin, A. A. Chemical storage of renewable energy. *Science* 360, 707-708, (2018).

9. Won, D. H. et al. Highly Efficient, Selective, and Stable CO₂ Electroreduction on a Hexagonal Zn Catalyst. *Angew. Chem. Int. Ed.* 55, 9297-9300, (2016).
10. Kim, H. et al. Identification of Single-Atom Ni Site Active toward Electrochemical CO₂ Conversion to CO. *J. Am. Chem. Soc.* (2021).
11. Zheng, T., Jiang, K. & Wang, H. Recent Advances in Electrochemical CO₂-to-CO Conversion on Heterogeneous Catalysts. *Adv. Mater.* 30, 1802066, (2018).
12. Gu, J., Hsu, C.-S., Bai, L., Chen, H. M. & Hu, X. Atomically dispersed Fe³⁺ sites catalyze efficient CO₂ electroreduction to CO. *Science* 364, 1091-1094, (2019).
13. Li, X. et al. Single Cobalt Atoms Anchored on Porous N-Doped Graphene with Dual Reaction Sites for Efficient Fenton-like Catalysis. *J. Am. Chem. Soc.* 140, 12469-12475, (2018).
14. Zu, X. et al. Efficient and Robust Carbon Dioxide Electroreduction Enabled by Atomically Dispersed Sn^{δ+} Sites. *Adv. Mater.* 31, 1808135, (2019).
15. Chen, J. et al. Efficient electroreduction of CO₂ to CO by Ag-decorated S-doped g-C₃N₄/CNT nanocomposites at industrial scale current density. *Mater. Today Phys.* 12, 100176, (2020).
16. Wang, Y. et al. Advanced Electrocatalysts with Single-Metal-Atom Active Sites. *Chem. Rev.* 120, 12217-12314, (2020).
17. Cheng, Y. et al. Atomically Dispersed Transition Metals on Carbon Nanotubes with Ultrahigh Loading for Selective Electrochemical Carbon Dioxide Reduction. *Adv. Mater.* 30, e1706287 (2018).
18. Jiang, K. et al. Isolated Ni single atoms in graphene nanosheets for high-

- performance CO₂ reduction. *Energy Environ. Sci.* 11, 893-903, (2018).
19. Zhang, H. et al. A Graphene-Supported Single-Atom FeN₅ Catalytic Site for Efficient Electrochemical CO₂ Reduction. *Angew. Chem. Int. Ed.* 58, 14871-14876, (2019).
 20. Li, K. et al. Visualizing highly selective electrochemical CO₂ reduction on a molecularly dispersed catalyst. *Mater. Today Phys.* 19, 100427, (2021).
 21. Zhu, Q. et al. Carbon dioxide electroreduction to C₂ products over copper-cuprous oxide derived from electrosynthesized copper complex. *Nat. Commun.* 10, 3851, (2019).
 22. Ringe, S. et al. Double layer charging driven carbon dioxide adsorption limits the rate of electrochemical carbon dioxide reduction on Gold. *Nat. Commun.* 11, 33, (2020).
 23. Wang, X. et al. Dynamic Activation of Adsorbed Intermediates via Axial Traction for the Promoted Electrochemical CO₂ Reduction. *Angew. Chem. Int. Ed.* 60, 4192-4198, (2021).
 24. Liu, T., Zhang, L., Cheng, B. & Yu, J. Hollow Carbon Spheres and Their Hybrid Nanomaterials in Electrochemical Energy Storage. *Adv. Energy Mater.* Ahead of Print, (2019).
 25. Han, L. et al. Stable and Efficient Single-Atom Zn Catalyst for CO₂ Reduction to CH₄. *J. Am. Chem. Soc.* 142, 12563-12567, (2020).
 26. Wu, Z.-Y. et al. Electrochemical ammonia synthesis via nitrate reduction on Fe single atom catalyst. *Nat. Commun.* 12, 2870, (2021).
 27. Wu, J. et al. Densely Populated Isolated Single Co-N Site for Efficient Oxygen Electrocatalysis. *Adv. Energy Mater.* 0, 1900149, (2019).

28. Yamamoto, T. Assignment of pre-edge peaks in K-edge x-ray absorption spectra of 3d transition metal compounds: electric dipole or quadrupole? *X-Ray Spectrom.* 37, 572-584, (2008).
29. Douglas, C. D., Dias, A. V. & Zamble, D. B. The metal selectivity of a short peptide maquette imitating the high-affinity metal-binding site of E. coli HypB. *Dalton Trans.* 41, (2012).
30. Rossi, G., d'Acapito, F., Amidani, L., Boscherini, F. & Pedio, M. Local environment of metal ions in phthalocyanines: K-edge X-ray absorption spectra. *Phys. Chem. Chem. Phys.* 18, 23686-23694, (2016).
31. Pan, Y. et al. Design of Single-Atom Co-N₅ Catalytic Site: A Robust Electrocatalyst for CO₂ Reduction with Nearly 100% CO Selectivity and Remarkable Stability. *J. Am. Chem. Soc.* 140, 4218-4221, (2018).
32. Pan, F. et al. Unveiling Active Sites of CO₂ Reduction on Nitrogen-Coordinated and Atomically Dispersed Iron and Cobalt Catalysts. *ACS Catal.* 8, 3116-3122, (2018).
33. Morlanés, N., Takanabe, K. & Rodionov, V. Simultaneous Reduction of CO₂ and Splitting of H₂O by a Single Immobilized Cobalt Phthalocyanine Electrocatalyst. *ACS Catal.* 6, 3092-3095, (2016).
34. Han, J. et al. Reordering d Orbital Energies of Single-Site Catalysts for CO₂ Electroreduction. *Angew. Chem. Int. Ed.* 58, 12711-12716, (2019).
35. Han, N. et al. Supported Cobalt Polyphthalocyanine for High-Performance Electrocatalytic CO₂ Reduction. *Chem* 3, 652-664, (2017).
36. Geng, Z. et al. Regulating the coordination environment of Co single atoms for

- achieving efficient electrocatalytic activity in CO₂ reduction. *Appl. Catal. B* 240, 234-240, (2019).
37. Kornienko, N. et al. Metal-Organic Frameworks for Electrocatalytic Reduction of Carbon Dioxide. *J. Am. Chem. Soc.* 137, 14129-14135, (2015).
38. Zhang, X. et al. Highly selective and active CO₂ reduction electrocatalysts based on cobalt phthalocyanine/carbon nanotube hybrid structures. *Nat. Commun.* 8, 14675, (2017).
39. Lin, S. et al. Covalent organic frameworks comprising cobalt porphyrins for catalytic CO₂ reduction in water. *Science* 349, 1208-1213, (2015).
40. Pei, J. et al. N-Bridged Co-N-Ni: new bimetallic sites for promoting electrochemical CO₂ reduction. *Energy Environ. Sci.* (2021).
41. Wang, X. et al. Regulation of Coordination Number over Single Co Sites: Triggering the Efficient Electroreduction of CO₂. *Angew. Chem., Int. Ed.* 57, 1944-1948, (2018).
42. Deringer, V. L., Tchougréeff, A. L. & Dronskowski, R. Crystal Orbital Hamilton Population (COHP) Analysis As Projected from Plane-Wave Basis Sets. *J. Phys. Chem. A* 115, 5461-5466, (2011).
43. Chibowski, E. Surface free energy of a solid from contact angle hysteresis. *Adv. Colloid Interface Sci.* 103, 149-172, (2003).
44. Hursán, D. et al. Morphological Attributes Govern Carbon Dioxide Reduction on N-Doped Carbon Electrodes. *Joule*, (2019).
45. Li, X. et al. Selective visible-light-driven photocatalytic CO₂ reduction to CH₄

mediated by atomically thin CuIn₅S₈ layers. *Nat. Energy* 4, 690-699, (2019).

Acknowledgements

Y. Li. and B.W. contributed equally to this work. This work was supported by Zhejiang University. Y.L. acknowledges support of National Key R&D Program of China (2018YFA0209600) and the Natural Science Foundation of China (22022813, 21878268). Q.J. acknowledges the financial supports from the DNL Cooperation Fund, CAS (DNL201903) and the National Natural Science Foundation of China (No. 51701201). R.Z. acknowledges the support of National Key Research and Development Program of China (No. 2017YFB0702100), Part of the DFT calculations were performed using the computational resources provided by School of Materials Science and Engineering, Beihang University. The authors thank Prof. Liang Zhang from the Institute of Functional Nano & Soft Materials, Soochow University for support of original EXAFS data.

Contributions

Y. Li. and B. Wei contributed equally to this work. Y. Lu, and Y. Li. designed and supervised the experiment with assistance from L. Fan and L. Lei. R. Zhang led and B. Wei assisted the computational investigations. Y. Li synthesized catalysts, conducted electrochemical study, Y. Lu and Y. Li analyzed data. Y. Li and Q. Jiang performed the characterization of catalysts structure and catalysis products. Y. Li wrote the manuscript with the support from Z. Li and Y. Lu.

Competing interests

The authors declare no competing interests.

Additional information

Supplementary information is available for this paper.

Corresponding author

Correspondence to Zhongjian Li or Ruifeng Zhang or Yingying Lu.

Supplementary Files

This is a list of supplementary files associated with this preprint. Click to download.

- [Supplementaryinformation2.docx](#)